



Study of room temperature NO₂ sensing performances of ZnO_{1-x} (x = 0, 0.05, 0.10)

M. Benamara¹ · J. Massoudi² · H. Dahman¹ · A. Ly³ · E. Dhahri² · M. Debliquy⁴ · L. El Mir¹ · D. Lahem³

Received: 5 September 2021 / Accepted: 30 November 2021 / Published online: 10 December 2021
© The Author(s), under exclusive licence to Springer-Verlag GmbH, DE part of Springer Nature 2021

Abstract

Zinc oxide nanopowder was made using an auto-combustion method, and oxygen vacancies were formed using a thermally activated procedure under vacuum treatment. The structural and morphological properties of ZnO_{1-x} samples were determined by using X ray diffraction (XRD), Raman spectroscopy, X-ray photoelectron spectroscopy (XPS), and scanning electronic microscope (SEM) characterizations. XRD studies revealed that the ZnO_{1-x} samples had a hexagonal wurtzite structure, with nanoparticle sizes ranging from 40 to 47 nm. The growing quantity of oxygen vacancies was confirmed by XPS tests. SEM images showed a spherical nanometric particle with high porosity especially for ZnO_{0.90}. Optical measurements with spectroscopy UV–Visible revealed that oxygen vacancies increase absorption of the material in the visible region. Also, the photoluminescence properties of the prepared samples were investigated by PL and PLE measurement, which indicate a high presence of oxygen vacancies and other defaults in the structure of ZnO_{0.90} more than pure zinc oxide. The electrical conductivity proportional to the temperature showed that the conduction process was thermally activated and that the carriers had long-distance mobility. Thus, we found that the conductivity of ZnO_{0.90} was lower than that of ZnO, which can be explained by the introduction of oxygen vacancies which allows the creation of electron trapping centers localized by the presence of the deep-levels. Spraying an aqueous solution of ZnO_{1-x} nanoparticles over alumina substrates with pre-deposited gold interdigitated electrodes resulted in gas sensors. At ambient temperature and under white light illumination, the manufactured sensors showed excellent sensing responses to 0.5 ppm NO₂. The presence of oxygen vacancies improves sensor performance, which the sensor based on ZnO_{0.90} showed a high response of 76.

Keywords ZnO_{1-x} · Room temperature NO₂ sensing · Electrical conductivity · X-ray photoelectron

1 Introduction

Nitrogen dioxide (NO₂) is a toxic and hazardous gas as it can have a negative influence on the health of human beings at elevated NO₂ concentrations in ambient air can cause chronic lung disease and respiratory infections [1]. It is imperative

to strengthen the monitoring of NO₂ to protect the health of people and promote the sustainable development of the society [2]. The signal is a simple variable resistance measured by a pair of electrodes deposited on an insulating substrate and covered by the sensitive material. These sensors easily fit into conventional electronic circuits. Moreover, this type of sensor is particularly suitable for the use of the current microfabrication technologies.

The exploited sensitive layers can consist of a mineral semiconductor, essentially metal oxides, or an organic semiconductor. Metal oxide gas sensors are so far the most used materials because of their competitive advantages: low cost, high sensitivity, quite long lifetime, simplicity of preparation, in-line monitoring potential and reproducibility in practical applications [3]. For the detection of NO₂, several types of metal oxides have been studied such as ZnO [4], NiO [5], SnO₂ [2], WO₃ [6], In₂O₃ [7], CuO [8], Fe₂O₃ [9]. Thanks to its numerous advantages such as its low cost,

✉ M. Benamara
majdibenamara1@gmail.com

¹ Laboratory of Physics of Materials and Nanomaterials Applied at Environment (LaPhyMNE), Faculty of Sciences in Gabes, Gabes University, 6072 Gabes, Tunisia

² Laboratoire de Physique Appliquée, Faculté des Sciences, Université de Sfax, B. P. 1171, 3000 Sfax, Tunisia

³ Materia Nova, Materials R&D Centre, Parc Initialis, Avenue Nicolas Copernic 3, 7000 Mons, Belgium

⁴ Service de Sciences des Matériaux, Université de Mons, Rue de l'Épargne 56, 7000 Mons, Belgium

high sensitivity, wide band gap energy (3.37 eV) and large exciton binding energy (60 meV), ZnO-based gas sensors have been intensively studied [10]. ZnO also exhibits high conduction electron mobility, high dopant solubility, non-toxicity, and good thermal stability [11, 12]. Ca-, In-doped and Ca–In-codoped ZnO-based sensors had been used to enhance CO and CO₂ gas detection performances when operating temperature was in the range between 150 and 500 °C [13]. Traditional ZnO gas sensors typically operate at high temperature (between 150 and 500 °C) because the adsorption–desorption phenomena are usually slow at room temperature leading to very long response or recovery times and low sensitivity. However, the high operating conditions pose several problems, such as distortion of sensor stability, high current consumption... [14]. Moreover, the development of ZnO gas sensors at a low temperature is promising because it saves energy consumption and does not require a heating element for high temperature operation, temperature-resistant substrates and packaging which simplifies the design of the sensor and thus reduces its manufacturing cost. Several researchers have reported that zinc oxide is one of the most interesting materials for NO₂ detection which exhibits excellent response to this gas even at low concentration [15].

To activate the surface reactions, it was proposed to use light as the source of energy instead of heat. In the case of ZnO, pristine ZnO has a large band gap (3.37 eV), so it is active only under ultraviolet (UV) illumination [16]. The UV light source usually requires customization that is difficult to obtain and can damage the sensor components or decompose the tested gases (it is precisely the case for NO₂) [17]. It is however interesting to reduce the band gap energy of ZnO sensor material or to dope it to extend the light absorption to shorter wavelengths, in the aim to allow the sensors to react in the visible light region [18]. It has been reported that implanting oxygen vacancies in ZnO effectively reduces its band gap [19]. It has also been shown that the oxygen deficiency has a strong effect of oxidative gas adsorption site and that the detection reactivity of the ZnO surface gas will be improved as its oxygen deficiency concentration increases [20]. Therefore, the preparation of ZnO sensitive materials with oxygen deficiency is an effective approach to improve the detection performance at ambient temperature. The oxygen vacant ZnO had good NO₂ responses under light illumination [18].

In this study, we have prepared ZnO nanoparticles, using autocombustion method, and then, the as-obtained product was treated with a thermally activated process to create oxygen vacancies in their structure and therefore obtain ZnO_{1-x} nanopowders. Three samples have been prepared: as-obtained ZnO and treated nanopowders with two oxygen vacancies concentrations, ZnO_{0.95} and ZnO_{0.90} which correspond to x=0.05 and 0.1, respectively. We have

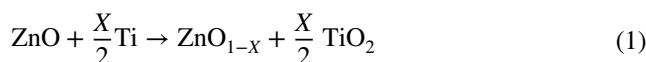
investigated the structural, morphological, optical, and electrical proprieties of all samples by XRD, Raman, SEM and UV–Visible spectroscopy, PL and impedance spectroscopy characterizations. Moreover, the performance and sensing properties of ZnO_{1-x} sensors toward 0.5 ppm NO₂ gas have also been investigated.

2 Experimental details

2.1 Preparation of nanoparticles

Pure zinc oxide was prepared by autocombustion method. Analytical grade zinc acetate dihydrate [Zn(CH₃COO)₂·2H₂O; 99%] and glycine (NH₂CH₂COOH) were completely dissolved in distilled water until a homogeneous solution is obtained. Glycine was used as a fuel with a ratio (1:2) taken according to stoichiometries proportion of zinc acetate. The aqueous solution was then stirred for about 1 h to mix the solution uniformly. By using hotplate, the mixed solution was evaporated on at 80 °C under constant magnetic stirring and concentrated by heating when the excess of water was evaporated with the formation of a viscous gel. The viscous gel was ignited by raising the temperature to 300 °C. The loose and burned powder samples were obtained. The burnt powder was calcined at 600 °C for 7 h. Finally, the synthesized nanopowders were ground for 1 h.

In order to create vacancies in oxygen sites, the prepared ZnO compound was placed in a quartz tube which contains a portion of metallic Titanium. The tube was sealed under vacuum and heated at 600 °C for 1 week. The ZnO_{1-x} samples were obtained from parental oxide, ZnO by extracting oxygen. ZnO was placed in a quartz tube with 5 mm in diameter and 15 mm in length. The present tube was introduced in a second quartz tube (8 mm diameter and 30 mm length) containing a stoichiometric proportion of metallic titanium which has the role of absorbing oxygen described by the following equation:



with X=0.05 and 0.10 in this work.

The external tube was pumped for a primary vacuum (10⁻³ Torr), sealed and annealed at 600 °C for one week. The oxygen deficiency, X, was measured using an inductively coupled plasma spectrometer.

In order to control the reaction, the products obtained were equilibrated by ultra-micro balance and the rate of oxygen vacancies was determined according to the following equation:

$$X = \frac{\Delta m \cdot M_{\text{mol}}}{m_{\text{used}} \cdot M_{\text{O}}} \quad (2)$$

where

Δm : Mass difference in the compound before and after the reaction,

M_{mol} : Molar mass of the stoichiometric ZnO compounds,

m_{used} : Weight of the used ZnO compounds,

M_{O} : Atomic mass of oxygen.

2.2 Sensor fabrication and measurements

250 mg of the prepared nanopowders was dispersed in 2.25 ml of distilled water. The prepared solution was then sonicated during 15 min until a uniformly dispersed suspension was obtained. The suspension is then deposited at 200 °C by spray technique on alumina substrates (Al₂O₃)

equipped with a pair of interdigitated gold electrodes on one side and a Pt heating coil on the back side (Fig. 1a). The fabrication steps of the sensor are more explained in Fig. 1b.

The gas detection tests were carried out using a home-made gas system consisting of a Teflon cell containing the sensors flown by a mixture of gases (Fig. 1c). The mixture of gases was prepared by mixing gases from cylinders with the help of flow controllers driven by a computer. The total gas flow is kept at 1 l/min. The humidity is generated in a bubbler. The sensors are linked to an electrical board to operate the sensors in a controlled temperature and perform resistance measurements while varying the concentration of nitrogen dioxide. To activate the sensors, a white LED lamp was placed in the cell in front of the sensors. The light intensity was 3 mW/cm². The relative sensitivity of the sensor is defined as the ratio $S = (R_{\text{gas}} - R_{\text{air}}) / R_{\text{air}}$ where R_{air} and R_{gas} are, respectively, the electrical resistance of the sensor, with

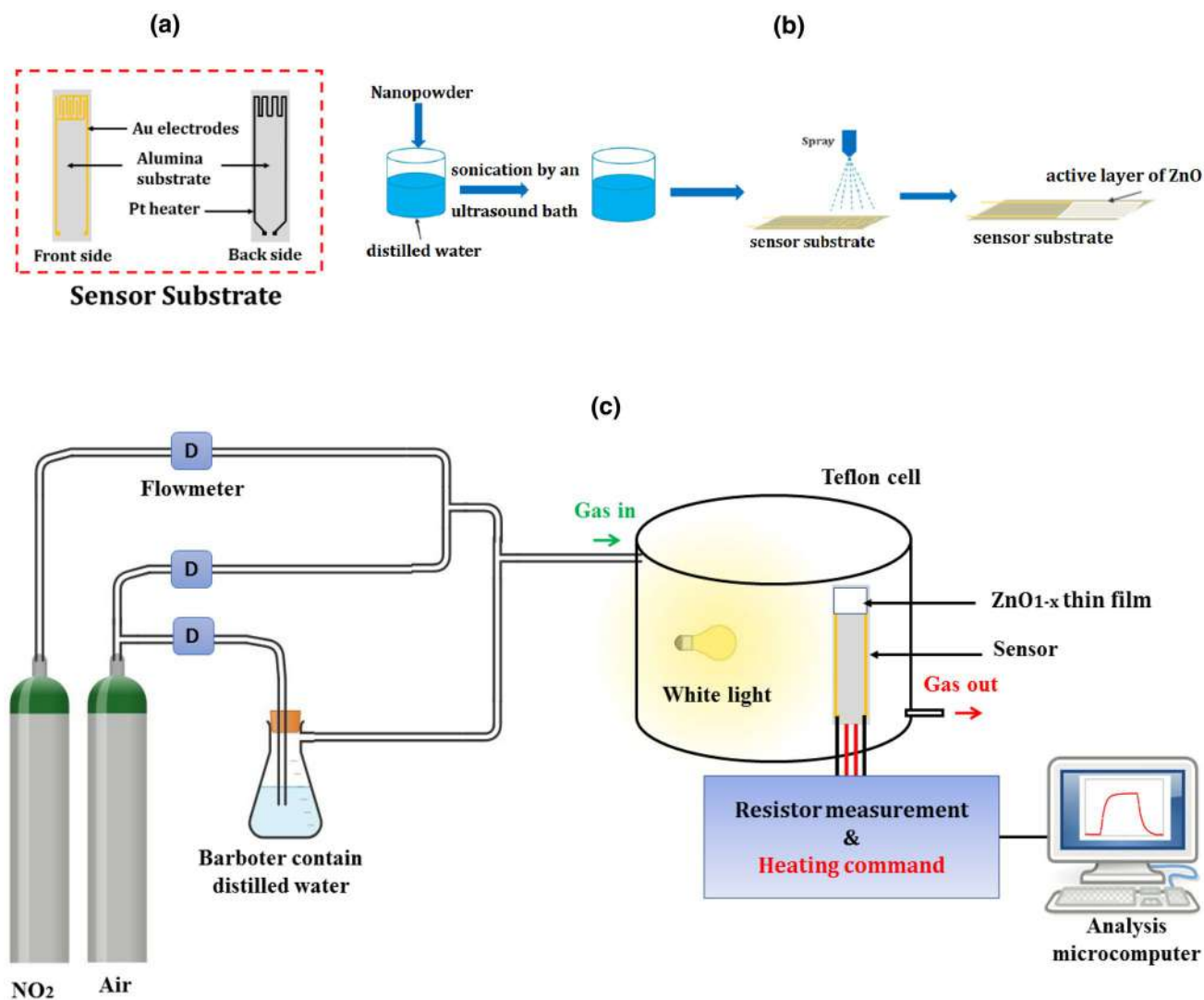


Fig. 1 a Sensor substrate. b The steps for fabrication of gas sensor. c Synoptic of gas testing station

50% relative humidity in the air, and at different target NO₂ gas concentrations. The response and recovery times were evaluated at 90% of the resistance change after exposure to the target gas and back to air, respectively.

2.3 Characterization measurements

To obtain information about, crystalline structure, morphology, optical and electrical properties, we have performed the measurements by X-ray diffraction (XRD), Raman spectroscopy, scanning electronic microscopy (SEM), photoelectron spectrometry (XPS), UV–Visible–NIR spectra, photoluminescence (PL), and impedance spectroscopy. The crystal structure of the prepared ZnO powder was detected by X-ray diffractometer (XRD, D8 Advance, Bruker AXS, Germany) and Jobin–Yvon Raman spectrometer with green exciting light ($\lambda = 532$ nm). The morphology of the synthesis nanopowders and the phase constitution were observed by field-emission scanning electron microscopy (FE-SEM, S4800II, Hitachi, Japan) and X-ray photoelectron spectroscopy (XPS, ESCALAB 250Xi, Thermo Scientific, USA), respectively. The light absorption and reflection properties were carried out using UV–Visible spectrophotometer (Shimadzu UV-3101PC) in the wavelength range of 200 to 800 nm. For PL and PLE measurement, a NanoLog Horiba modular spectrofluorometer was used which it was equipped with an Xe lamp with 330 nm excitation light source wavelength. An Agilent 4294 analyzer was used to extract the electrical properties of the samples. It was investigated in the temperature range between 200 and 310 K and the frequency of the applied ac field is between 100 Hz and 1 MHz. Those measurements were done in a helium atmosphere in order to improve the heating transfer and avoid moisture.

3 Results and discussion

3.1 XRD and SEM characterizations

XRD analysis was performed to study the microstructure of non-stoichiometric zinc oxide nanopowders. The average size (D) of the crystallites was calculated using Debye–Scherrer's equation.

The obtained D values for all samples are ranging between 40 and 47 nm and presented in Table 1. The X-ray diffraction patterns of the ZnO_{1-x} ($x = 0, 0.05$ and 0.10) nanoparticles are further refined using Rietveld analysis using fullproof program [21] and are shown in Fig. 2a–c. The values of different structural parameters are calculated and listed in Table 1. The obtained refined lattice parameters confirm the formation of hexagonal wurtzite structure (hcp) ZnO with the P63mc space group. The oxygen vacancies do not lead to the appearance of any extra peaks

Table 1 Structural, optical, and electrical parameters of ZnO_{1-x} samples

Parameter	ZnO	ZnO _{0.95}	ZnO _{0.90}
a (Å)	3.2493	3.2502	3.2503
c (Å)	5.2049	5.2052	5.2059
V (Å ³)	47.589	47.618	47.630
c/a	1.6018	1.6015	1.6016
R	0.9999	0.9998	0.9999
χ^2	1.81	10.53	6.17
R _p (%)	8.87	12.30	9.43
R _{wp} (%)	11.0	13.4	9.8
R _e (%)	8.19	4.12	3.94
S (m ² /g)	24.00	22.70	26.96
$\rho_{x\text{-ray}}$ (g.cm ⁻³)	5.67915	5.6199	5.56275
$\epsilon \cdot 10^{-5}$	89	5.5	15
D _{W-H} (nm)	61.35	72.5	49.5
D _{TEM} (nm)	83	98	42
E _g (eV)	3.17	3.22	3.23
E _u (meV)	22	25	31
E _a (meV)	88	65	72

or the disappearance of any peak related to the hexagonal wurtzite structure of pure ZnO, which indicated that all samples have high crystalline purity. The low value of χ^2 shown in Table 1 suggests that the refining of the samples is effective and that the samples obtained are of good quality. The unit cell volume is calculated via [22]:

$$V = 0.866 * a^2 * c \quad (3)$$

It is clear from Table 1 that the size of lattice parameters a and c and the volumes of the unit cell slightly increase on increasing the oxygen vacancies due to a linear mismatch of ionic size between in a tetrahedral coordination. Moreover, the oxygen vacancies may change the lattice parameters values, but the crystal system (hexagonal) and space group (P63mc) remain unchanged. However, the perfect wurtzite unit cell has a hexagonal configuration with two network parameters, a and c, with c/a ratio equal to 1.633. The distortion degree ($R = 1.633$ a/c) can calculate the deviation of crystal from the perfect arrangement, where $R = 1$ gives an ideal wurtzite structure with $c/a = 1.633$ [22]. The value of the degree of distortion R suggests that the oxygen vacancies do not change the wurtzite structure. In this work, the obtained value of the c/a ratio is listed in Table 1. Further, the crystallite size and lattice strain of the ZnO nanoparticles were evaluated using a well-known Williamson–Hall (W–H) method [23]. Representative Williamson–Hall plots of ZnO_{1-x} samples are shown in Fig. 2e, f–sg. The plot between $\beta \cos \theta$ and $4 \sin \theta$

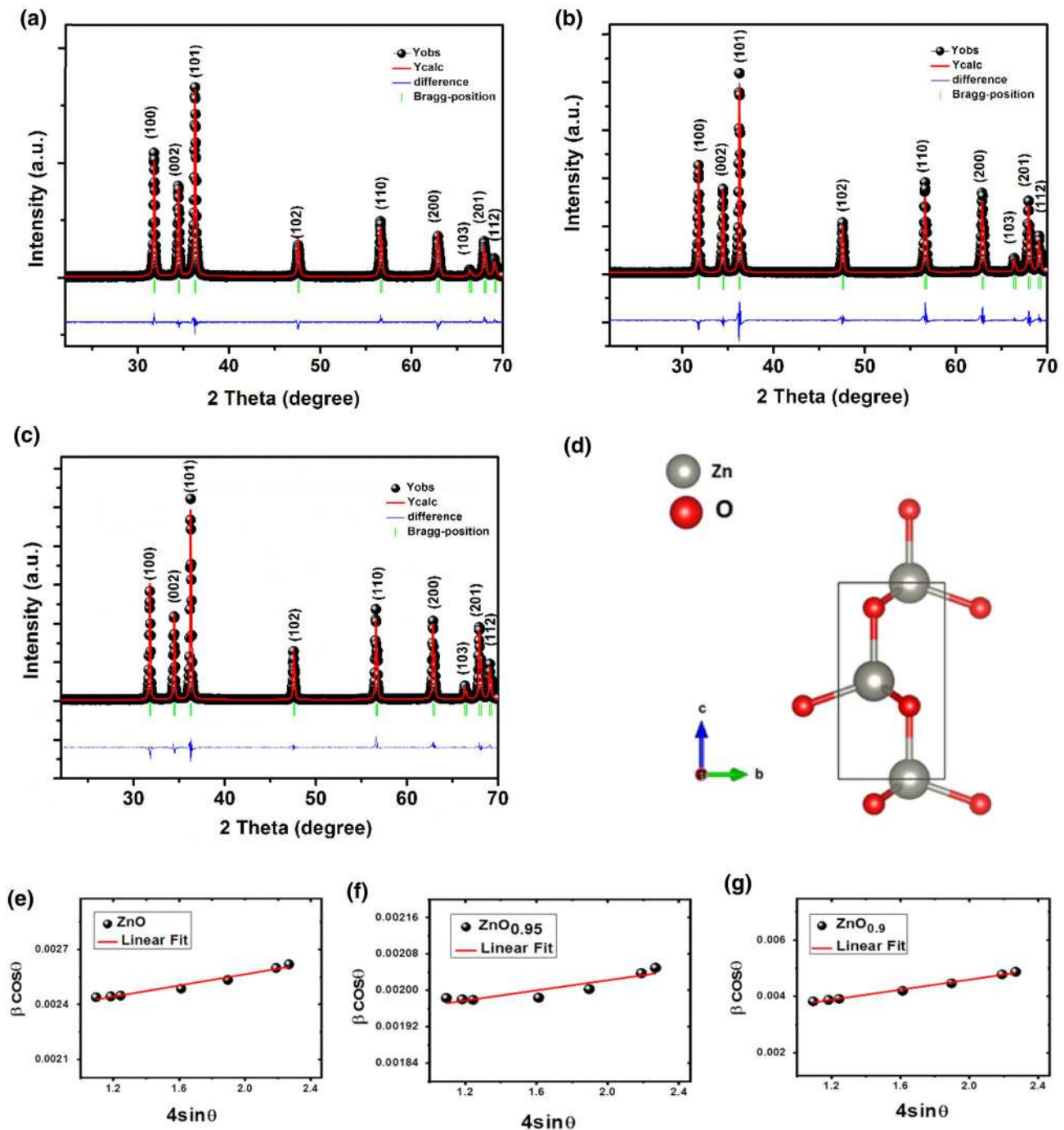


Fig. 2 Rietveld refined X-ray diffraction patterns of ZnO_{1-x} nanoparticles with **a** $x=0$, **b** $x=0.05$, **c** $x=0.10$. **d** The unit cell of the ZnO sample. Williamson–Hall plot for **e** ZnO, **f** ZnO_{0.95} and **g** ZnO_{0.90} samples

provides the strain through the slope of the line and particle size (D_{WH}) can be evaluated from the intercept of the line (on the y axis). Average crystallite sizes, for all synthesized samples, calculated by using Scherrer's formula and the Williamson–Hall plot are presented in Table 1. As can be seen in Table 1, the average crystallite size estimated from the Scherrer equation is quite different from

that obtained by the W–H plot. This difference between the average crystallite size estimated from the Scherrer equation and from the W–H plots can be explained by the fact that the micro-stress can induce a larger widening of the diffraction peak, whereas in the Scherrer equation, the total width of the diffraction peak is taken into account in the calculation. X-ray density ($\rho_{X\text{-ray}}$) of the samples was

calculated by considering that a basic unit cell of the cubic spinel structure contained eight ions using the following equation [23]:

$$\rho_{X\text{-ray}} = \frac{2M}{N_A V} \quad (4)$$

where M is the molecular weight of each compound, N_A is the Avogadro's number, V is the volume and 2 represents the number of molecules in a unit cell of the hexagonal wurtzite lattice (Fig. 2d). The X-ray density decreased almost in a linear way with the increase in the oxygen vacancies. This can be explained on the fact that the X-ray density is directly related to the molar mass and inversely related to the unit cell volume of the material. Assuming all the nanoparticles to be spherical, the specific surface area is calculated from the relation [23]:

$$S = \frac{6000}{D \cdot \rho_{X\text{-ray}}} \quad (5)$$

where the constant 6000 is called form factor for spherical particles, D is the diameter of the particle. The auto-combustion process is known for synthesizing materials with high surface area (S). However, it is interesting to note that the high surface area of nanoparticles is needed for sensing applications [24].

To determine further information about the effect of oxygen vacancies on the change in crystal structure of ZnO, measurements of Raman spectra are also performed and shown in Fig. 3. There are two peaks observed with high intensity located at 100 and 440 cm^{-1} which represent the two modes of atomic displacement E_{2L} and E_{2H} attributed to the typical characteristic ZnO [25]. Meanwhile, a new vibrations mode located at 194 and 520 cm^{-1} was also observed, which were attributed to oxygen vacancies [26,

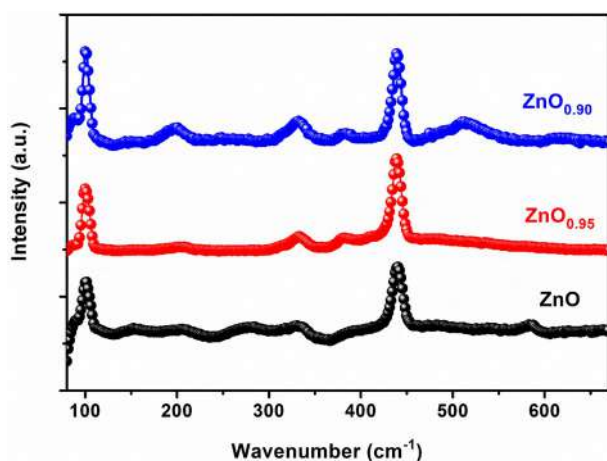


Fig. 3 Raman spectra of ZnO_{1-x} (with $X=0, 0.05$ and 0.10)

27]. Moreover, it can be observed that the peak intensity at 194 and 520 cm^{-1} was increased except $\text{ZnO}_{0.90}$. The highest peak intensities were obtained in $\text{ZnO}_{0.90}$ indicating the maximum oxygen vacancy concentration.

The morphology of ZnO samples has been studied by SEM analysis and the results with nanoparticles size distributions are shown in Fig. 4. The obtained images indicate porous materials and the presence of agglomerates composed by non-uniform distribution of hexagonal shape grains, sized between 33 and 100 nm. This result is expected because grain, with morphology commonly determined by SEM, may be formed by an agglomeration of crystallites. Therefore, in the most probably case, the crystallite is smaller than a grain. Table 1 presents the crystallite and grain size of all ZnO_{1-x} samples deduced from XRD and SEM investigations. The SEM images reveal a smaller grain size of $\text{ZnO}_{0.90}$ nanopowders. By comparison with particle size values estimated from SEM (Table 1), the average particle size agrees with the average crystallite size estimated from W–H model. Therefore, the W–H model is more suitable method than the Scherrer's formula in the present study.

3.2 XPS spectra measurement

X-ray photoelectron spectroscopy (XPS) is considered one of the most important materials characterization techniques to have information about elemental identification, chemical state of elementary and relative composition of the constituents in the surface region. XPS was recorded using Al $K\alpha$, as a source with $h\nu = 1486.6$ eV under a vacuum of about $2 \cdot 10^{-6}$ Pa. The XPS was calibrated using sputtered references material Ag (for peak position, work function), Au and Cu (for retard linearity). Charge compensation was done using dual compensation (electron and very low energy ion gun (Ar)). Charge compensation was checked using a reference PET sample. The spectra corresponding to the O1s and the Zn2p3 of the ZnO_{1-x} samples are calibrated by the binding energy of the C1s (284.6 eV) as internal reference spectra [28]. However, it is worthwhile noticing that recently a study of XPS measurements outlined certain controversy concerning the choice of the binding energy of C1s as reference in XPS spectra, because of the dispersion observed in the C1s binding energy which may depend on the carbon source used taken as reference [29]. XPS was used to characterize all prepared samples, and results are presented in Fig. 5 for oxygen and zinc elements. The O1s spectrum was deconvoluted and fitted using the Lorentzian composite function. The spectra O1s core level of all samples ZnO_{1-x} , shown in Fig. 5, indicates the presence of two peaks, in all samples, centered at 529.87–530.26 and 531.16–531.71 eV, which are attributed to the presence of O^{2-} ions in Zn–O bonding of ZnO wurtzite structure and to oxygen-deficient regions in the matrix, respectively, of

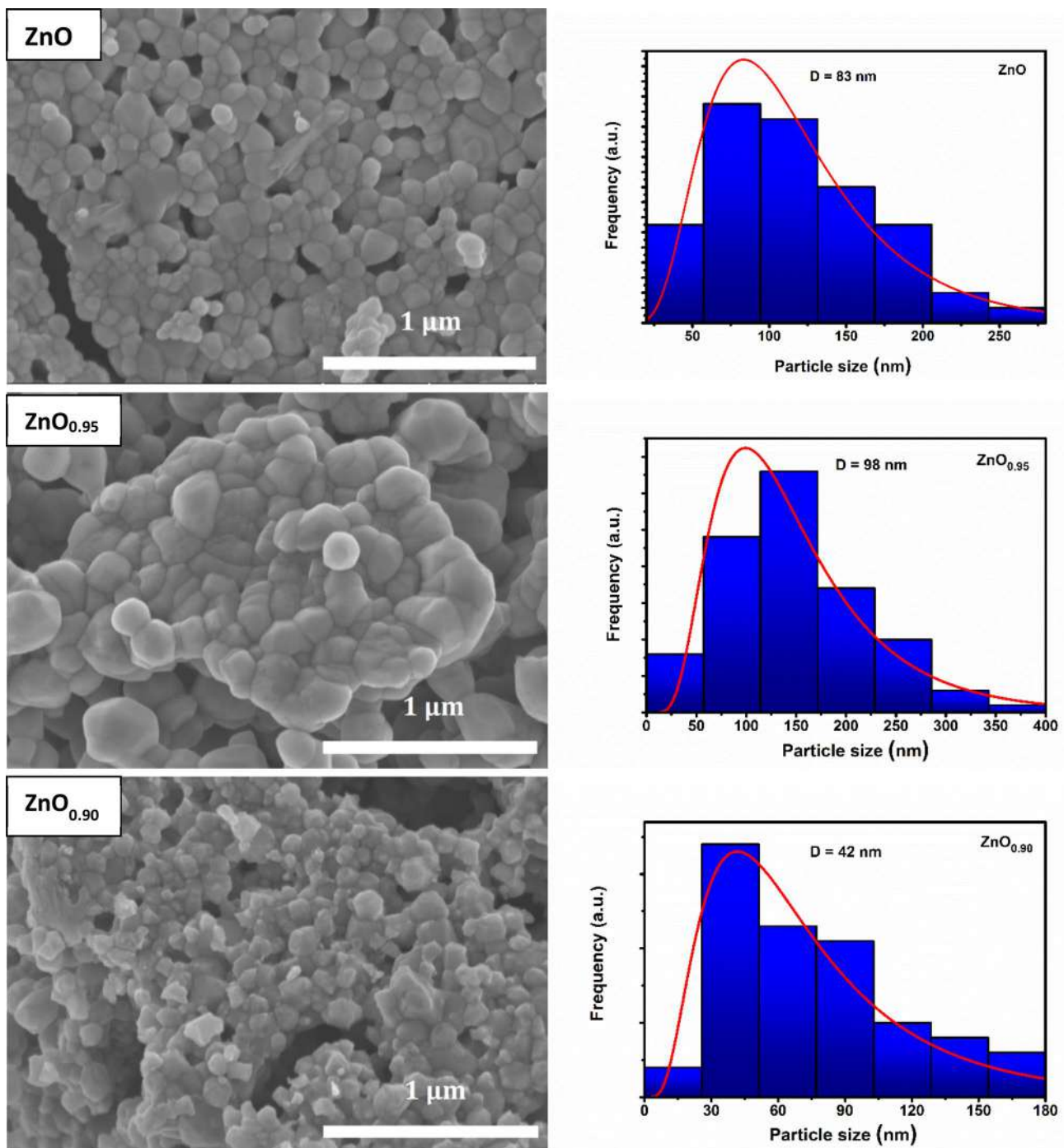


Fig. 4 SEM images and the representative histograms of size distribution for ZnO_{1-x} samples

our ZnO_{1-x} samples [30]. The pure ZnO presents a supplementary peak with lower binding energy (528.3 eV) which is attributed to oxygen in =CO groups [31]. The calculation of the ratio between peak related to oxygen vacancy to the total O1s spectral area of ZnO, ZnO_{0.95} and ZnO_{0.90} samples gives, respectively, 0.156, 0.231 and 0.414 proving the increasing concentration of oxygen vacancies. Those

oxygen vacancies may play an important role for the electrical properties, as well as for their gas sensing properties as they act as preferential adsorption sites. The obtained ratio values may indicate that ZnO_{0.90} coatings had maximum oxygen vacancy concentration. We have also shown the XPS spectra of Zn2p3 core level in Fig. 5. Very similar shape of Zn2p3 core levels was observed and peaks

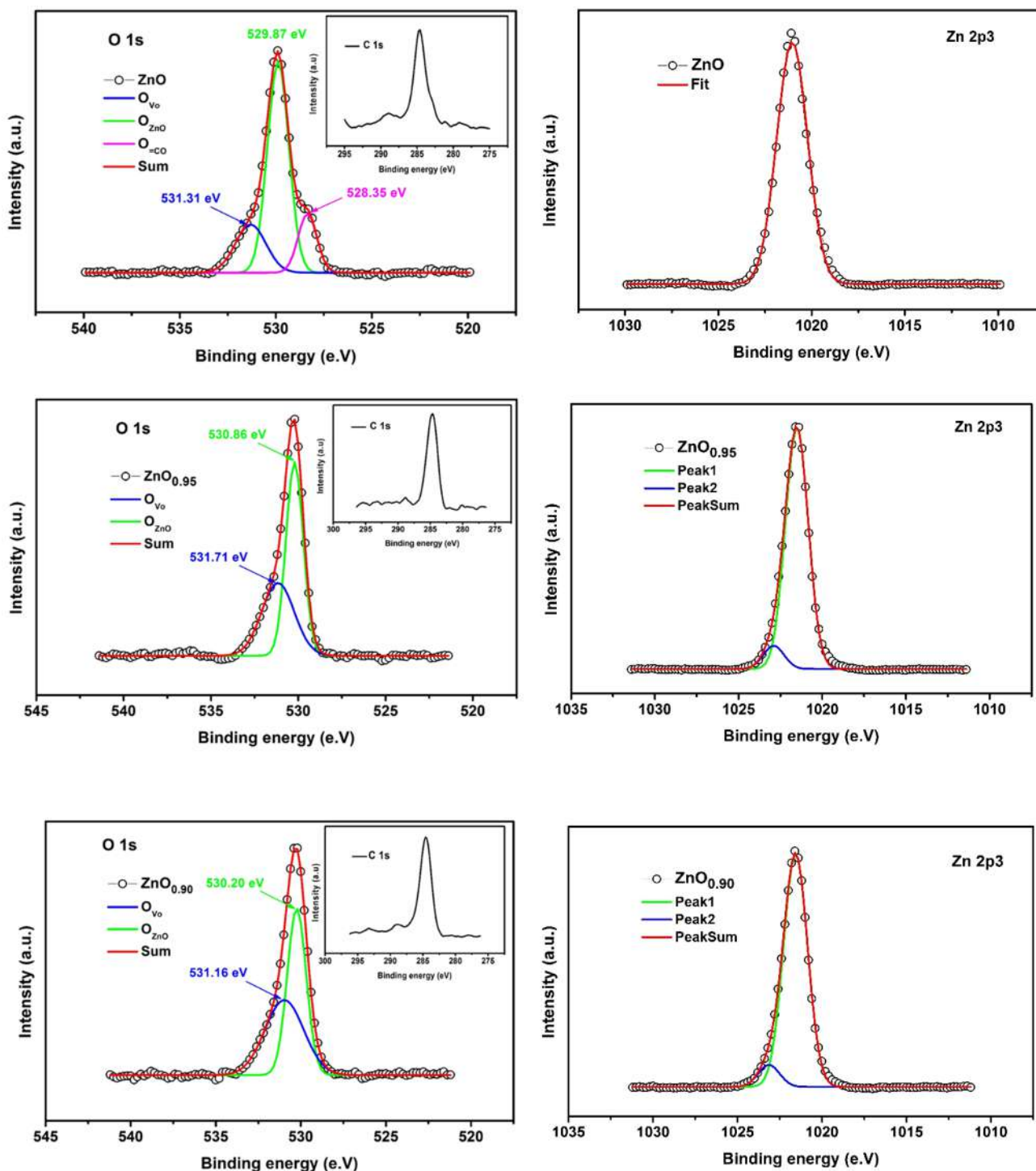


Fig. 5 XPS spectra: O 1s with C 1s (inset) and Zn 2p3 of the ZnO_{1-x} samples

centered at 1021.1, 1021.6 and 1021.6 eV for ZnO, ZnO_{0.95} and ZnO_{0.90}, respectively. It indicates the presence of Zn²⁺ in the structure of ZnO [32]. The main core level Zn 2p3 spectra of ZnO_{0.95} and ZnO_{0.90} centered at ~ 1021.6 eV show slightly asymmetrical features, as shown in Fig. 5, respectively. This behavior indicates the existence of Zn in

its multiple-oxidation states. The deconvoluted Zn 2p3 core levels XPS spectra show two peaks: for ZnO_{0.95}, it was centered at ~ 1021.52 eV and ~ 1022.90 eV and for ZnO_{0.90}, it was centered at ~ 1021.56 eV and ~ 1023.14 eV. These peaks were corresponding to different oxidation states of Zn. The lower energy peak in the deconvoluted spectrum is attributed

to the network of Zn²⁺ ions surrounded by O²⁻ ions in the hexagonal ZnO and is called the oxide form of Zn [33]. The deconvoluted peak centered on the side of the highest binding energy is linked to metallic zinc [34]. We can conclude, from the XPS of O1s and Zn2p3, that the elements O and Zn were detected from all samples. In addition, we have detected the presence of oxygen vacancies (V_O) for all samples.

3.3 Optical properties

The gas detection tests are carried out under visible light illumination; the optical properties of the ZnO samples must therefore be characterized to prove the extension of the absorption spectrum to the visible part of the spectrum. To highlight the effect of oxygen vacancies on light absorption, UV–Visible characterization has been performed on compressed powder disk, in the range 200–800 nm, and results concerning the absorbance curves are presented in Fig. 6a. Very high absorbance can be observed in the UV range (200–400 nm); however, for wavelengths higher than

400 nm, remarkable increasing in the absorbance may be observed with increasing oxygen vacancies. This behavior is probably due to the creation of energy levels between the valence and conduction bands, facilitating the transition of the electrons between the two bands, which then makes it possible to absorb more light [35].

The optical reflectance of the ZnO_{1-x} nanoparticles was measured at room temperature and illustrated in Fig. 6b. In the visible range, the reflectance decreases as a function of the increase in the rate of oxygen vacancies, which proves that the scattering power optics of this type of material is quite important in this range. In contrast, it is minimal in the UV range, which shows that absorption is highest in this region. The variation spectra of the first derivative of the reflectance as a function of the wavelength (λ) ($dR/d\lambda$) for the ZnO_{1-x} samples are shown in Fig. 6c. We can estimate the energy gap values which present an increase as a function of the increase in oxygen rate (Table 1). Therefore, the band gap was closely related to oxygen deficiency; it was enlarged according to the increase in oxygen

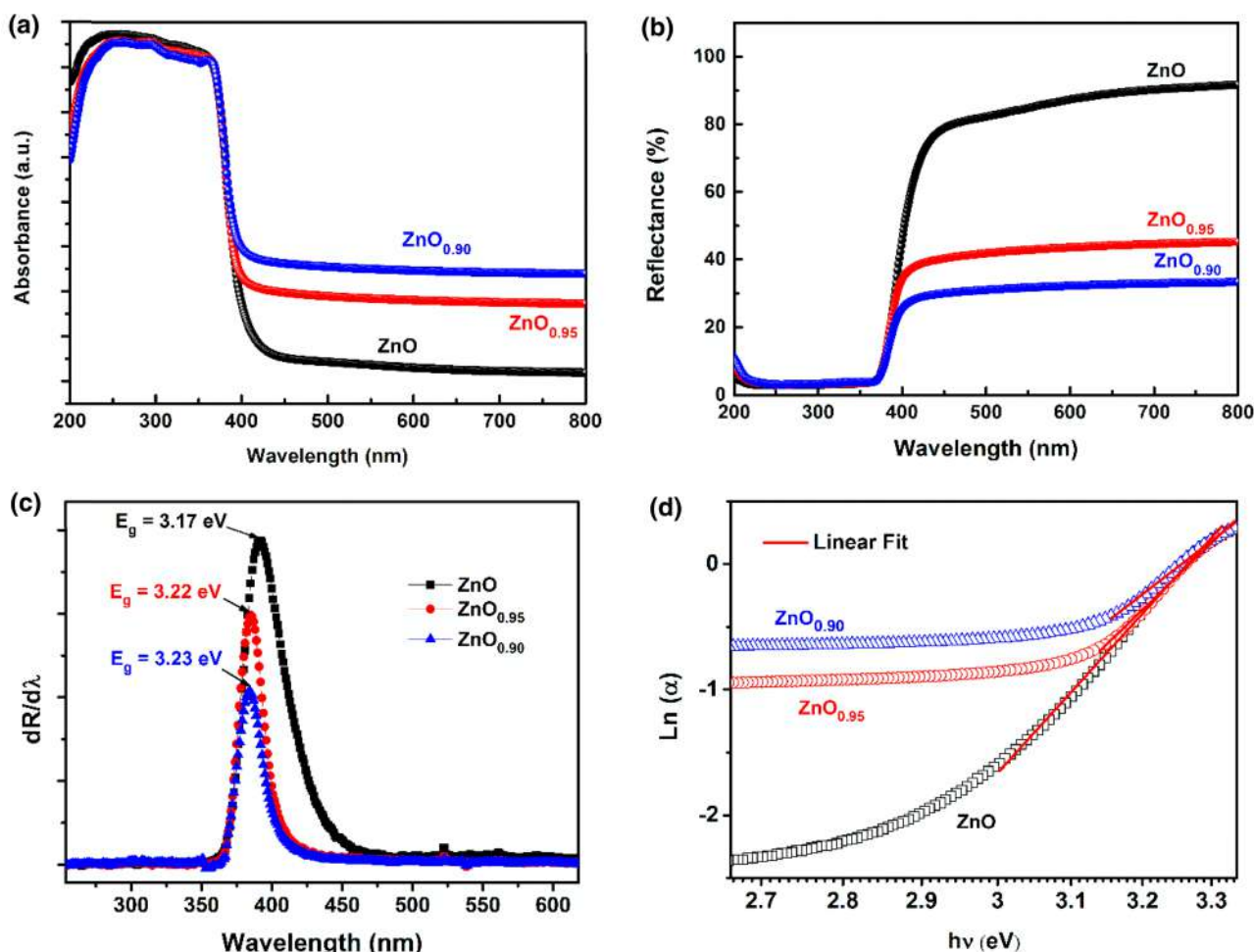


Fig. 6 **a** Absorbance and **b** reflectance spectra of ZnO_{1-x} samples. **c** $dR/d\lambda$ vs. wavelength and **d** $\text{Ln}(\alpha)$ vs. $h\nu$ of ZnO_{1-x} samples

vacancies. This can be explained by the effect of vacating oxygen sites. The valence band of transition metal oxide semiconductors mainly consists of the 2p orbital of O. The conduction band (CB) comes from the d orbital of the metal. Oxygen defects cause a change in the valence band of the semiconductor material (shifting upwards).

In fact, it is probable that the variation in the parameters of the crystal lattice causes the creation of states of electronic imperfections in the forbidden band. The localized defect near the valence (BV) and conduction (BC) two bands created several energy levels in the form of a tail band called Urbach energy [36]. According to Urbach's law, we can estimate Urbach's energy from the following equation.

$$\ln(\alpha) = \ln(\alpha_0) + \frac{E_u}{hv} \quad (6)$$

where E_u and α_0 are the Urbach energy and a constant, respectively [37]. The curves of $\ln(\alpha)$ as a function of $h\nu$ are presented in Fig. 6d. The estimated E_u values, for the ZnO_{1-x} samples, are the inverses of the slopes of the linear part of the curves and they are presented in Table 1. The E_u value increases for the samples with oxygen vacancies. Compared to pure ZnO, this implies the creation of other defects due to the presence of vacant sites.

The PL spectra of ZnO_{1-x} are studied and shown in Fig. 7. Gaussian fit was used to deconvolute the normalized PL spectra. It is clear from the curve in Fig. 7 that the ZnO pure has a large band in the visible range which shows a green emission refer to the oxygen vacancies (V_o) and zinc interstitial (V_{Zn}) [38], and an orange-red emission attributed to an excess of oxygen [39]. The deconvoluted curve of $\text{ZnO}_{0.95}$, shown in Fig. 7, indicates a shift in which there is a more big green emission and a little orange-red emission which indicate the creation of more of oxygen vacancies (V_o) and less oxygen interstitial. For the sample $\text{ZnO}_{0.90}$, the disappearance of orange-red and a high green emission confirmed a high presence of oxygen vacancies in our structure [40].

The PLE spectra of ZnO_{1-x} samples, in the UV range, were also studied. Figure 7 presents the PLE spectra deconvoluted by a Gaussian equation of ZnO, $\text{ZnO}_{0.95}$, and $\text{ZnO}_{0.90}$, respectively. Figure 7 shows the deconvolution of the PLE spectrum of ZnO by several peaks (290 nm, 343 nm, 365 nm and 375 nm). The first peak at 292 nm (4.25 eV) is attributed to the excitonic emission confined. A large peak at 343 nm (3.61 eV) is also present with two other peaks at 365 nm (3.39 eV) and 375 nm (3.31 eV) which are redshifted from the exciton emission. There is a shift toward higher wavelength for the samples treated by oxygen vacancy defects ($\text{ZnO}_{0.95}$ and $\text{ZnO}_{0.90}$) which refer to the reducing of the gap energy and subsequently the presence of many defects in the structures of treated zinc oxide such as oxygen vacancies and interstitials of zinc [41].

3.4 Electrical property

We propose to detect the electrical properties of ZnO_{1-x} compounds to highlight the impact of the creation of the oxygen deficiency. The ac conductivity spectra of the ZnO_{1-x} samples are shown in Fig. 8a. The electrical conductivity strongly depends on the variation in the frequency. Increasing the frequency serves to increase the conductivity of each sample. While the electrical conductivity decreases with increasing oxygen deficiency rates, this is due to the high presence of charge carrier trapping centers in the samples $\text{ZnO}_{0.90}$ and $\text{ZnO}_{0.95}$ compared to pure ZnO. We can conclude that oxygen vacancies could act as charge carrier traps. Also, conductivity measurements are carried out in dc mode, in a wide temperature range [200–310 K]. Also, the dependence of the conductivity dc (σ_{dc}) on the temperature is shown in Fig. 8b. The observed increase in σ_{dc} with temperature showed that the conduction process was thermally activated and that the carriers had long-distance mobility. Likewise, we found that the conductivity of $\text{ZnO}_{0.90}$ was lower than that of ZnO, which can be explained by the introduction of oxygen vacancies which allows the creation of electron trapping centers localized by the presence of the levels. Deep free Zn^{2+} ions or oxygen vacancies (single or double ionized) caused the creation of those levels. Therefore, the increase in conductivity was related to the increase in the concentration of electrons at shallow depth. In addition, the increase in oxygen deficiencies led to increases in local interior stresses. Thus, it is clear that the representative curve of $\ln(\sigma)$ as a function of $1000/T$, presented in Fig. 8b, is an affine line segment and hence Arrhenius law can be applied to determine the activation energy of this conduction mechanism [42]. The expression of Arrhenius law making it possible to adjust the dependence of the conductivity (σ) on the temperature is as follows:

$$\sigma \cdot T = A \exp\left(-\frac{E_a}{k_B T}\right) \quad (7)$$

where is the pre-exponential factor, E_a is the activation energy, k_B is the Boltzmann constant ($k_B = 8.617 \cdot 10^{-5}$ eV. K^{-1}) and T is the temperature. The good linear behavior suggests that the conduction mechanism is thermally activated. The values of the activation energy (E_a) determined by fitting the curves in Fig. 8c are grouped together in Table 1. Referring to electrical neutrality, the increased oxygen deficiency in the system leads to an increase in the number of Zn^{2+} ions. This increase is accompanied by an improvement in the mechanism of the double-exchange interaction (DE), therefore, a reduction in the activation energy.

The Nyquist diagrams of the samples ZnO and $\text{ZnO}_{0.90}$ at room temperature are presented in Fig. 9a. The appearance of the semicircles indicates the semiconductor behavior of

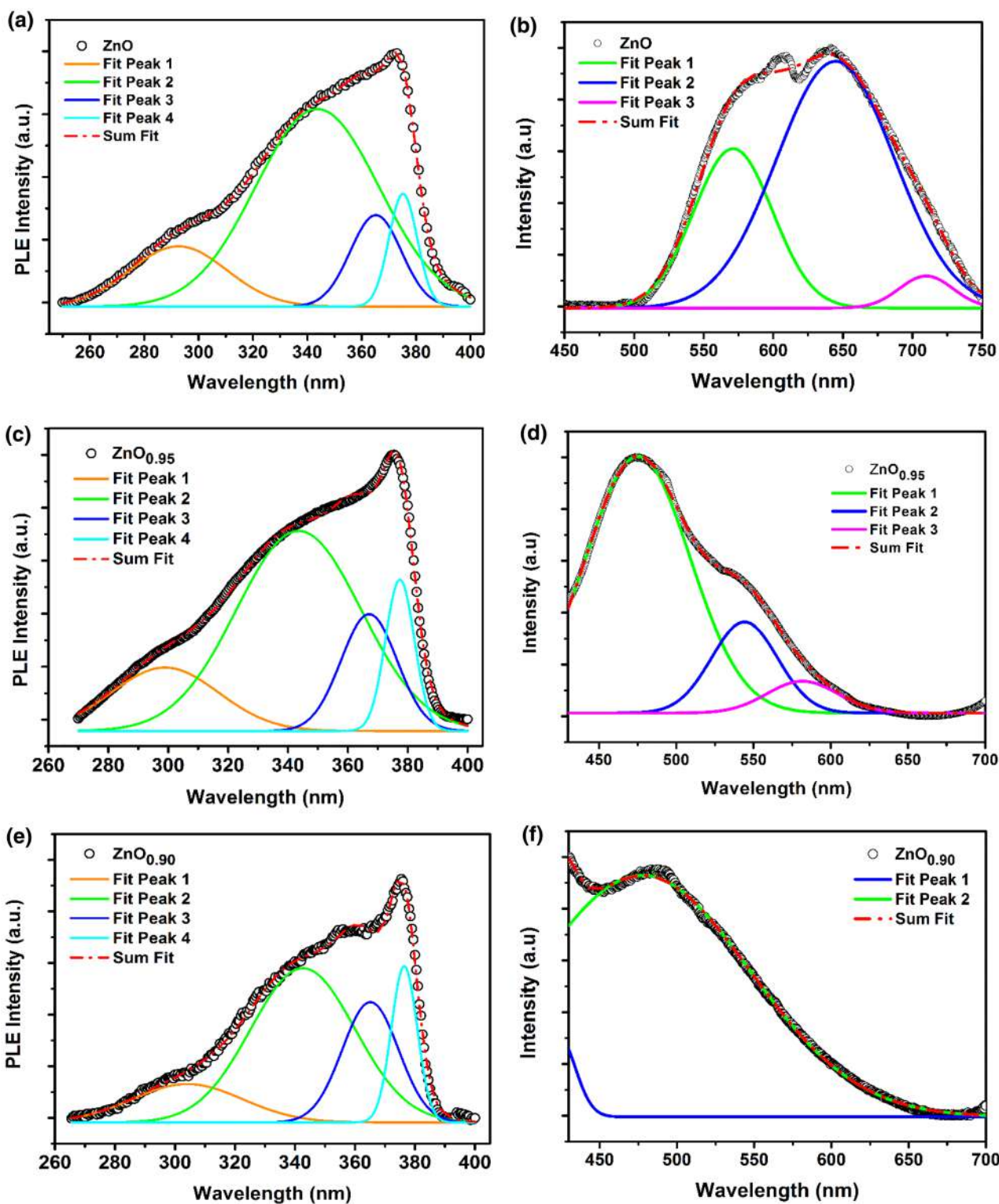


Fig. 7 PLE Spectra of a ZnO, c ZnO_{0.95}, and e ZnO_{0.90} samples. PL Spectra of ZnO_{1-x} with b x=0.00, d x=0.05, and f x=0.10

the samples in the temperature considered. The resulting semicircles were centered below the Z' axis indicating a non-Debye dielectric relaxation which can be attributed to

the heterogeneity of the material. The electrical responses of the ZnO_{1-x} samples are modeled by an equivalent circuit formed by a two-series combination of grain boundary

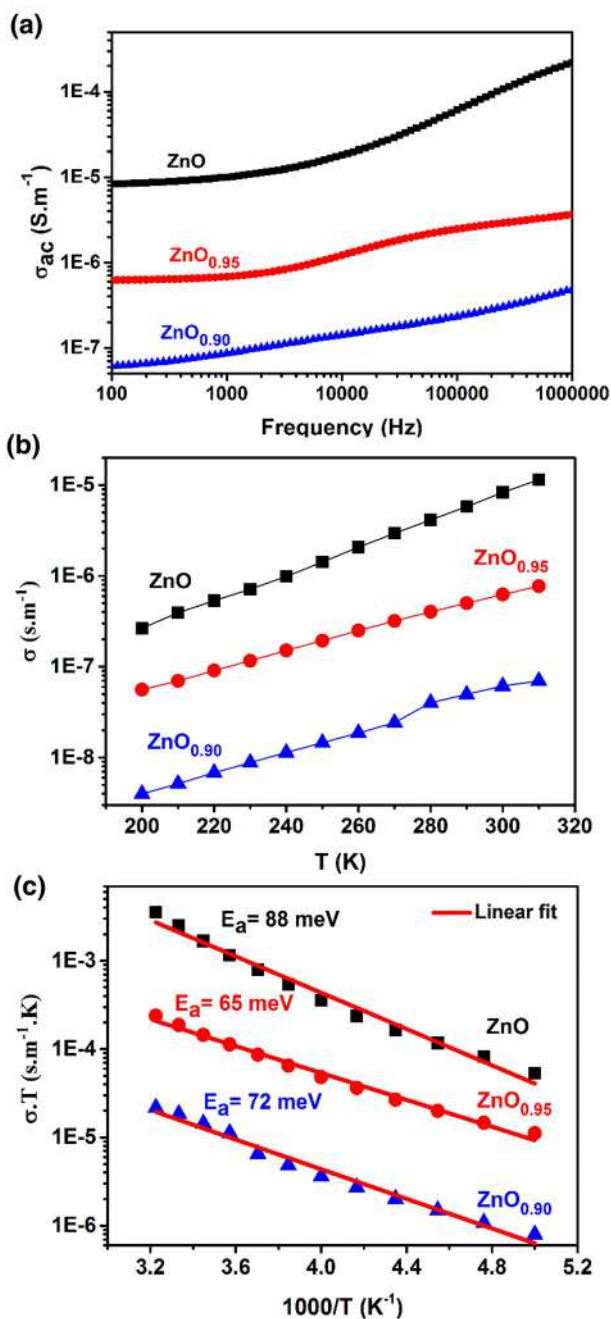


Fig. 8 a Frequency dependence of σ_{ac} , b Temperature dependence of σ and, c $\sigma \cdot T$ vs. $1000/T$ for ZnO_{1-x} samples

resistance-grain boundary capacity (R_{gb} -CPE_{gb}) and grain resistance (R_g). According to the Koops model [43], the conductivity of a semiconductor is governed by grain boundaries, at low frequencies (right side) and highly conductive grains, at high frequencies (left side). The ZnO_{0.90} sample shows a semicircle of larger diameter compared to that of ZnO. This indicates the presence of oxygen deficiencies for the ZnO_{0.90} sample which can play the role of grain boundaries.

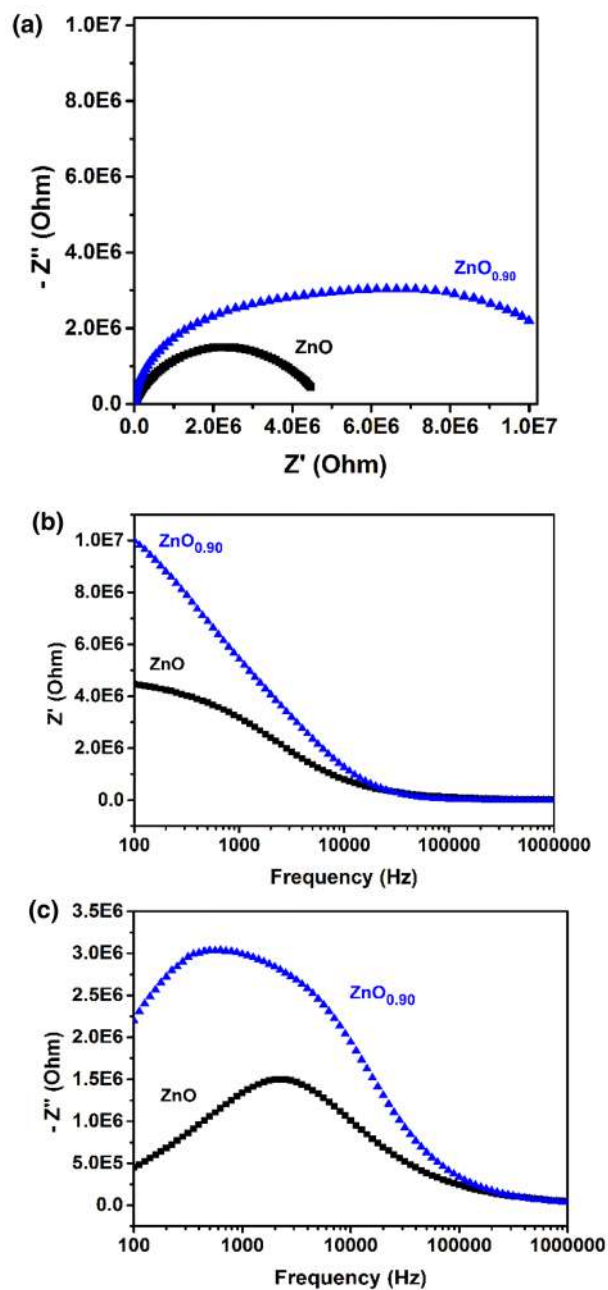


Fig. 9 a Nyquist diagram of ZnO_{1-x} samples. Frequency dependence of b Z' and (c) Z'' of the ZnO_{1-x} nanoparticles

The spectra of the impedance real part (Z') for the samples ZnO and ZnO_{0.90} are presented in Fig. 9b at low frequency, Z' is maximum for the two samples and it decreases sharply as a function of the increase in frequency value. At high frequencies, Z' exhibits minimal values due to the presence of space charge polarization. For ZnO_{0.90}, Z' has a large value compared to that of ZnO. This behavior is linked, mainly, to the presence of more barriers due to the introduction of oxygen vacancies. The vacancies improve the surface

effect, the formation of interfaces, and the Schottky barriers to contacts. Figure 9c shows the spectra of the imaginary part of the impedance (Z''), for the samples ZnO_{1-x}, at room temperature. Each curve presents a relaxation peak which depends on the relaxation frequency which attributes to the mobility of the jump charge carriers. The presence of grain boundaries, which are generally more resistive than grains and due to the presence of oxygen vacancies and dangling bonds at grain boundaries, causes active charge carrier traps in the structure of the material. Therefore, grain responses are expected to occur at higher frequencies compared to those of grain boundaries. Thus, the ZnO relaxation peak is present at high frequencies compared to that for ZnO_{0.90} which is present at low frequencies. This behavior can confirm the high presence of oxygen vacancies for the ZnO_{0.90} samples compared to the parent compound.

3.5 NO₂ sensing tests

The synthesized powders were sprayed on alumina substrate to fabricate chemoresistive sensors. The room temperature ZnO_{1-x} resistances vs. time, to 0.5 ppm NO₂ under white light illumination, are shown in Fig. 10. Under a white light illumination, the base resistance decreased as the oxygen vacancy concentration increased (Table 2). The electrical resistance of pure zinc oxide is higher than those with oxygen vacancies. The significant reduction in

Table 2 Room temperature sensing characteristics of ZnO_{1-x} sensors under 0.5 ppm NO₂ with white light illumination

Sample	Resistance in air (Ohm)	Response	Response time (min)	Recovery time (min)
ZnO	8.33 10 ⁵	22	1.30	5.8
ZnO _{0.95}	5.78 10 ⁵	45	1.95	3.1
ZnO _{0.90}	3.89 10 ⁵	76	1.50	2.7

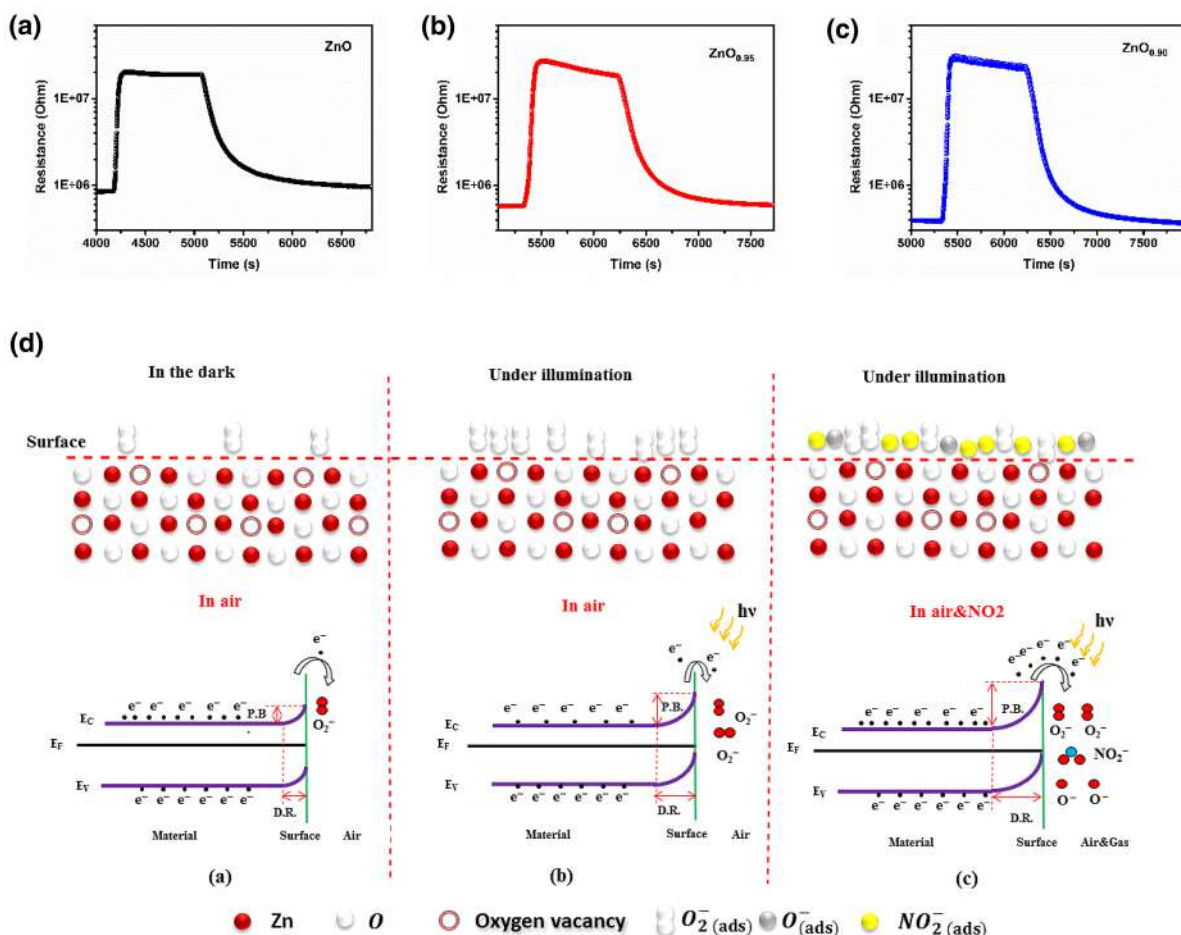


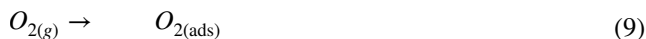
Fig. 10 Sensor resistances vs. time under white light illumination of ZnO_{1-x} sensors with **a** X=0.00, **b** X=0.05 and, **c** X=0.10. Schematic illustration of the gas sensing mechanism for ZnO_{1-x} gas sensor exposed in air and transferred to NO₂ atmosphere, illuminated by white light

electrical resistance is mainly due to the presence of oxygen vacancies which act as donors. The oxygen vacancies concentration had a remarkable influence on the electrical properties of the ZnO samples. As can be seen, from this figure, all tested samples are sensitive to nitrogen dioxide under white light illumination. The samples with oxygen default have a good response and better than pure sample such as shown in Fig. 10b and c. Furthermore, all samples with oxygen default have a response and recovery times smaller than those of pure zinc oxide. The response and recovery times of ZnO_{1-x} samples are given in Table 2.

Oxygen plays a very important role in the gas detection mechanism for ZnO. At room temperature, when ZnO_{1-x} is exposed to air, the O₂ molecules can adsorb on the surface and capture electrons from the ZnO_{1-x} conduction band becoming then ionized to O₂⁻, O⁻ and O²⁻ species [44]. O₂⁻ is mainly the majority specie when the operating temperature is below than 150 °C, while O⁻ and O²⁻ become the majority for a temperature above 150–200 °C [45]. As the global resistivity of the layer is conditioned by the contact resistance between the grains, the conductance for this kind of structure can be expressed by:

$$G = G_0 \exp\left(-\frac{eV_s}{k_B T}\right) \quad (8)$$

where G₀ is a constant, eV_s is the potential barrier and k_B is the Plank constant. Equation (8) shows the role of the potential barrier which is directly linked to the amount of adsorbed molecule par surface unit. These reactions are explained by the following relationships [46]:



Under light and at room temperature, dioxygen (O₂) is adsorbed on the surface of the material to form light-generated oxygen ions, O₂⁻ (hv), which capture electrons from the conduction band following the equation:



But the opposite reaction (photodesorption) also happens.



The process of generating oxygen vacancies is mainly accompanied by physical/chemical changes, for example, changes in the Fermi level, breaking and reshaping of links, and distortion of the crystalline network. The presence of oxygen vacancies in the structure of ZnO could create a new sub-level energy in which the concentration of oxygen vacancies reaches more than 0.1%, the energy bands can be

profoundly modified compared to pure material. The valence band (VB) of the transition semiconductor metallic oxides consists mainly of the 2p O orbital. The conduction band (CB) comes mainly from the orbital d of the metal. Then, the presence of donor defects such as oxygen deficiencies provokes a change of the valence band (VB). These changes in the energy band cause changes in the optical absorption properties of the material.

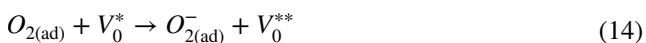
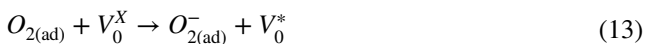
These defects were created; thanks to the non-stoichiometric relationship between the anions (O²⁻) and the cations (Zn²⁺) of ZnO material. Due to these defects, discrete energy levels have been introduced in the band gap of the material. Depending on the nature of the defect, the new levels can be donor or acceptor. Subsequently, the addition of defects causes the creation of additional charge carriers, free electrons, or holes. This induces changes in the electrical and optical properties of the material. For n-type metal oxides (eg ZnO), the levels formed by oxygen vacancies function as a bridge in the transition of electrons and act as donors levels of electrons. As a result, a new level of donor vacancy has been formed between valence and conduction bands [47].

The absorption of oxygen vacancies is important for the transition of electrons inside the material which are excited after having absorbed the energy of the photons [48]. Thereafter, less energy is introduced for the electronic transitions as the material has a wider range of visible light absorption, which is reflected in the macroscopic change in the color of the material. Oxygen vacancies in the material can also modify the surface reactivity, which influences the adsorption–desorption phenomena.

The mechanism for improving the electrical conductivity of semiconductor materials can be summarized in two aspects: the presence of oxygen vacancies can accelerate the rate of charge carrier transport (electrons in our case) [25], the presence of vacancies of oxygen can increase support concentration within the material [49]. Under light illumination, the oxygen vacancies present at the interface act as electron trapping sites gathering many electrons, which allow having a metallic conductivity in the material. Consequently, the presence of oxygen vacancies has reconstructed an electronic interface which produces metallic conduction and subsequently allows an increase in the rate of conduction of the charge carriers. Under illumination, the different concentrations of oxygen vacancies have effects on the conductivity of the material: The higher the concentration of oxygen vacancies, the higher the conductivity of the metal oxide.

In this context, oxygen vacancies are considered as donor defects. So, they are strong adsorption sites for oxygen molecules [19, 50]. Increasing oxygen vacancies concentration can increase the number of adsorption sites per unit of area. Then, more oxygen species O₂⁻ will be adsorbed on the ZnO_{1-x} coatings by taking electrons from the CB of ZnO,

which significantly reduce the number of free electrons. The following expressions may be used to describe this:



By illumination with white light, even though ZnO cannot be excited, the donor levels.

resulted by oxygen vacancies are excited to generate free electrons in the conduction band. Therefore, V_o^x ionized into V_o° and V_o^{oo} by releasing electrons in the conduction band as explain by reactions (15) and (16) [51, 52].

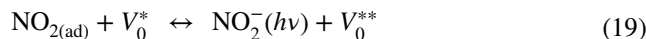
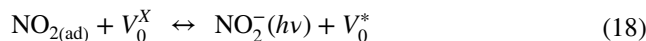


Those electrons can participate to photo-adsorption processes and to conduction that is why the resistivity decreases under illumination and thus why the sensitivity is increased. These results indicate that the sensitivity, the response and recovery rates were improved when oxygen vacancy concentration was increased. Under white light illumination, oxygen vacancy V_o^x would positively charge V_o° and V_o^{oo} by releasing electrons into the conduction band which was beneficial for the chemisorption of gas molecules. Thus, more O_2^- molecules can be adsorbed on the vacant oxygen surface than a stoichiometric molecule with fewer electrons [53].

The light effect on the detection mechanism is considered by the change in electrical resistance. The ZnO sensor was exposed to air in the dark condition; the free electrons in the conduction band have been captured by oxygen species adsorbed on the surface of ZnO and subsequently create a depletion layer.

The global resistance is high. After illumination, photodesorption takes place, electrons are released, and the resistance decreases (see Table 2). Of course, the effect is most visible in for the sample with more oxygen vacancies. The electron affinity of NO₂ is higher than that of oxygen [54] and the trap is a deeper meaning that when NO₂ replaces oxygen on the surface, the energy barrier is even higher. The adsorption energy of NO₂ molecules on metal oxides containing oxygen vacancies is much lower than that on pure oxides, which reveals that NO₂ molecules could be chemisorbed to a surface containing vacant sites in oxygen more easily [51]. Therefore, oxygen deficiency has been shown to be a suitable site for oxidative gases [36, 47]. In addition, when the oxygen vacancy concentration increased, more NO₂⁻ species may readily adsorb to the sample surface by capturing the electrons of the CB, resulting in a higher and more rapid response. When NO₂ is injected, the light-generated NO₂⁻(hv) molecules, since it is a reducing gas, formed

by capturing electrons photo-generated from oxygen vacancies or from O₂⁻ (hv) (oxygen is replaced by NO₂) due to the electronic affinity difference is larger for NO₂ (2.27 eV for NO₂ and 0.44 eV for O₂) [54]. In the first time, NO₂ can be adsorbed in the ZnO_{1-x} surface by capturing electrons from conduction band and reacting with neutral or simple ionized oxygen vacancies via the following equations:



In the second time, NO₂ can reacted with oxygen species (O₂⁻) adsorbed on the surface and with electrons from the surface to give NO₂ and O⁻ adsorbed species on the surface via



The reaction presented in Eq. (20) caused more emission of the electrons from the material to the species adsorbed in the surface which that can increased the electrical resistance and so that increasing the sensor response. The detection mechanism, in the three cases (under air in the dark, under air in the illumination and under air & NO₂ in the illumination), is more explained in Fig. 10d in which we have explained the role of oxygen vacancies in the NO₂ sensing mechanism.

In the illumination condition, the short response time is due to the photodesorption process of the oxygen species which may induce the release of the trapped electrons on the adsorbed NO₂⁻ species. Always, the illumination can help to increase the adsorption and desorption kinetics and therefore reduce the response and recovery times. After illumination, shortest response time is due to the photodesorption process which may induce the release of the trapped electrons on the adsorbed NO₂⁻ species. We can deduce that the presence of oxygen vacancies improves the NO₂ detection performance at room temperature. The introduction of oxygen vacancies can form optical traps which improve the absorption capacity of white light and allow to have a high efficiency of use of light in ZnO.

Table 3 shows the room temperature performances of ZnO_{0.90} and other ZnO-based NO₂sensors studied in the literature. According to C. Zhang et al. [53], investigations, conducted at room temperature under white light illumination, on ZnO_{0.952}-based sensor, revealed a response of approximately 5.3 toward 0.9 ppm NO₂ concentration, with 2.7 and 1.8 min as recovery and response times, respectively. It is worthwhile noticing that lower oxygen vacancy sensors: ZnO_{0.957}, ZnO_{0.963} and ZnO_{0.981} exhibited lower

Table 3 Performances of ZnO_{0.90} as room temperature (RT) NO₂ sensor in comparison with ZnO literature results

Materials	Fabrication method	Light illumination/ sensing temperature	NO ₂ (ppm)	Response (R _{NO₂} -R _{air})/ R _{air})	Response/Recov- ery times (min)	References
ZnO	H ₂ O ₂ treatment & annealing	White/RT	0.9	5.3	1.8/2.7	[49]
ZnO	Print screened thin film& annealing	-/200 °C	5	400	1.68/0.9	[50]
ZnO	Liquid plasma spray	-/300 °C	1	9.2	8.7/over 20	[58]
ZnO	Drop-cast	UV/RT	5	1.1	1.5/5	[53]
ZnO	Soft e-beam lithography	UV/RT	20	2.2	15/5	[54]
ZnO	Chemical deposited Thin film	-/RT	20	119	1.42/1.76	[55]
ZnO	Sputtering	UV/RT	0.5	8	-/-	[59]
ZnO nanorods	Hydrothermal method	UV/RT	0.5	8.9	2.5/3	[60]
ZnO nanowalls	Thermal reduction	-/RT	5	3.5	0.5/0.25	[61]
ZnO nanosheet	Thermal evaporation	UV/RT	1	2.1	0.25/4.5	[62]
ZnO nanowires	Hydrothermal method	UV/RT	1	7.1	0.5/2.5	[63]
ZnO	Auto-combustion	White/RT	0.5	76	1.5 /2.7	This work

responses 4.45, 4.08 and 2.57, respectively. However, an increase of response and recovery times was observed [53]. Higher, response 9.2, response and recovery times, respectively, equal to 8.7 min and over 20 min, were obtained on sprayed ZnO sensor for working temperature of 300 °C [55]. J. H. Jun et al. [54] obtained higher response 400 toward 5 ppm NO₂ gas in operating temperature of 200 °C, and the response and recovery times were, respectively, 0.17 and 0.22 min with no used activation light. These performances were obtained on the annealing sensor with patterned necked ZnO nanoparticles at 400 °C during 12 h. There is no doubt, that a high working temperature is a major inconvenience for a gas sensor, leading to the excessive energy consumption, and limitations of the places and use conditions. Furthermore, the high sensing temperature may affect the device life and the long-term stability, which makes room temperature as a working temperature, a main quality of a gas sensor. From given results in Table 3, and on focusing on room temperature sensors, and for all reported in the literature, NO₂ concentrations were less than 5 ppm, the responses were less than 8 ranging between 1.1 and 8, with response and recovery times in the range 0.5–1.8 min and 1.5–5 min, respectively. For higher concentration of 20 ppm of NO₂ gas, S. Fan et al. [56] reported a response of 2.2 and higher response and recovery times 15 and 5 min, respectively, obtained on sensor made by Soft e-beam lithography, even under UV activation light. R.K. Sonker et al. observed a high sensitivity 119 toward 20 ppm of NO₂ gas at room temperature, on nanopetal structured ZnO thin film sensor, fabricated by chemical route [57].

In our study, ZnO_{0.90}-based sensor exhibited best performances compared to the other fabricated ZnO_{1-x} sensors. It is important to note that the ZnO_{0.90} sample has the smallest grain size confirmed by SEM images and a relatively higher

absorption in the visible range, which may give it a better specific surface area and more effective light activation, leading to better sensitivity in the detection process. Furthermore, the observed behavior may also be related to an excess of free electrons, this assumption may be confirmed by the observed lower resistance of ZnO_{0.90} sensor. Higher specific surface area in nanostructured surface may play an important role in the adsorption mechanisms; however, on supposing sensitivity/ppm as comparing parameter, we can deduce that ZnO_{0.90} sensor has better performance, 152 against 5.95 for nanopetal structured ZnO thin film [57] and 80 for screen printed necked ZnO nanoparticles at 200 °C as working temperature [54].

4 Conclusion

In this study, ZnO_{1-x} was prepared by the auto-combustion method and treated by a thermally activated process, based on a vacuum treatment, to create oxygen vacancies in the structure of ZnO nanopowders with different percentages. X-ray diffraction measurements indicated that the structure of the pure and treated ZnO was hexagonal wurtzite and the size of nanoparticles was ranged between 40 and 47 nm. SEM images exhibited the presence of hexagonal agglomerates consisting of nanoscale particles. Optical investigations in the UV–Visible range highlighted higher absorption in visible range of treated ZnO samples and the band gap energy slightly increased from 3.17 to 3.23 eV with increasing oxygen vacancies. XPS measurements proved the increasing amount of oxygen vacancies. The electrical conductivity was proportional to the temperature which showed that the conduction process was thermally activated and that the carriers had long-distance mobility. The sensing

test under 0.5 ppm of NO₂ and white light illumination at room temperature was investigated and outlined an enhancement in sensors performances due to the presence of oxygen vacancies which may improve, under illumination, electrons pumping from the material to the interface. The obtained sensor performances seem to be promising for the development of low-cost room temperature NO₂ gas sensors.

References

- M.A. Chougule, D.S. Dalavi, S. Mali, P.S. Patil, A.V. Moholkar, G.L. Agawane, *Measurement* **45**, 1989–1996 (2012)
- G. Lu, J. Xu, J. Sun, Y. Yu, Y. Zhang, F. Liu, *Sens. Actuators B Chem.* **162**, 82–88 (2012)
- S. Jaballah, M. Benamara, H. Dahman, A. Ly, D. Lahem, M. Debliquy, L. El Mir, *Mater. Chem. Phys.* **255**, 123643 (2020)
- M. Benamara, J. Massoudi, H. Dahman, E. Dhahri, L. El Mir, A. Ly, M. Debliquy, D. Lahem, *J. Mater. Sci. Mater. Electron.* **31**(17), 14249–14260 (2020)
- S.J. Mezher, M.O. Dawood, O.M. Abdulmunem, M.K. Mejbel, *Vacuum* **172**, 109074 (2020)
- Y. Shen, T. Li, X. Zhong, G. Li, A. Li, D. Wei, Y. Zhang, K. Wei, *Vacuum* **172**, 109036 (2020)
- H. Bi, Y. Shen, S. Zhao, P. Zhou, S. Gao, B. Cui, D. Wei, Y. Zhang, K. Wei, *Vacuum* **172**, 109086 (2020)
- Y.H. Navale, S.T. Navale, F.J. Stadler, N.S. Ramgir, V.B. Patil, *Ceram. Int.* **45**(2), 1513–1522 (2019)
- N. Zahmouli, M. Hjiri, L. El Mir, A. Bonavita, N. Donato, G. Neri, S.G. Leonardi, *Nanotechnology* **30**(5), 055502 (2018)
- S. Jaballah, M. Benamara, H. Dahman, D. Lahem, M. Debliquy, L. El Mir, *J. Mater. Sci.: Mater. Electron.* **31**, 8230–8239 (2020)
- M. Benamara, E. Gómez, R. Dhahri, A. Serrà, *Toxins* **13**, 66–82 (2021)
- A. Bembibre, M. Benamara, M. Hjiri, E. Gómez, H.R. Alamri, R. Dhahri, A. Serrà, *Chem. Eng. J.* **13**, 2021 (2006)
- R. Dhahri, M. Hjiri, L. El Mir, E. Fazio, F. Neri, F. Barreca, N. Donato, A. Bonavita, S.G. Leonardi, G. Neri, *J. Phys. D: Appl. Phys.* **48**, 255503 (2015)
- S.A. Vanalakar, V.L. Patil, N.S. Harale, S.A. Vhanalakar, M. Gang, J. Kim, P.S. Patil, J. Kim, *Sens. Actuators B Chem.* **221**, 1195–1201 (2015)
- C. Zhang, X. Geng, H. Li, P. He, M. Planche, H. Liao, M. Olivier, M. Debliquy, *Mater. Res. Bull.* **63**, 67–71 (2015)
- Y. Chen, X. Li, J. Wang, Z. Tang, *Sens. Actuators B Chem.* **232**, 158–164 (2016)
- C. Zhang, J. Wang, M. Olivier, M. Debliquy, *Sens. Actuators B Chem.* **209**, 69–77 (2015)
- X. Geng, P. Lu, C. Zhang, D. Lahem, M.G. Olivier, M. Debliquy, *Sens. Actuators B Chem.* **282**, 690–702 (2019)
- L. Saadi, C. Lambert-Mauriat, V. Oison, H. Ouali, R. Hayn, *Appl. Surf. Sci.* **293**, 76–79 (2014)
- Y. Huang, M. Liu, Z. Li, Y. Zeng, S. Liu, *Mater. Sci. Eng. B* **97**, 111–116 (2003)
- J. Rodríguez-Carvajal, *Physica B* **192**(1–2), 55–69 (1993)
- D.K. Dubey, D.N. Singh, S. Kumar, C. Nayak, P. Kumbhakar, S.N. Jha, D. Bhattacharya, A.K. Ghosh, S. Chatterjee, *RSC Adv.* **6**(27), 22852–22867 (2016)
- D. Bouokkeze, J. Massoudi, W. Hzez, M. Smari, A. Bougoffa, K. Khirouni, L. Bessais, *RSC Adv.* **9**(70), 40940–40955 (2019)
- H. Trabelsi, M. Bejar, E. Dhahri, M.A. Valente, M.P.F. Graça, *Phys. E Low-dimension. Syst. Nanostruct.* **108**, 317–325 (2019)
- C. Zhang, X. Geng, J. Li, Y. Luo, P. Lu, *Sens. Actuators, B* **248**, 886–893 (2017)
- G. Exarhos, A. Rose, C. Windisch, *Thin Solid Films* **308–309**, 56–62 (1997)
- C. Youn, T. Jeong, M. Han, J. Kim, *J. Cryst. Growth* **261**, 526–532 (2004)
- J. Das, S.K. Pradhan, D.R. Sahu, D.K. Mishra, S.N. Sarangi, B.B. Nayak, S. Verma, B.K. Roul, *Physica B* **405**(10), 2492–2497 (2010)
- G. Greczynski, L. Hultman, *Prog. Mater. Sci.* **107**, 100591 (2020)
- H.L. Guo, Q. Zhu, X.L. Wu, Y.F. Jiang, X. Xie, A.W. Xu, *Nanoscale* **7**(16), 7216–7223 (2015)
- A. Celebioglu, S. Vempati, C. Ozgit-Akgun, N. Biyikli, T. Uyar, *RSC Adv.* **4**(106), 61698–61705 (2014)
- Y. Caglar, M. Caglar, S. Ilcan, *Optik* **164**, 424–432 (2018)
- U. Ilyas, R.S. Rawat, T.L. Tan, P. Lee, R. Chen, H.D. Sun, L. Fengji, *J. Appl. Phys.* **111**(3), 033503 (2012)
- U. Ilyas, P. Lee, T.L. Tan, R.V. Ramanujan, S. Zhang, R. Chen, H.D. Sun, R.S. Rawat, *Int. J. Mod. Phys. Conf. Ser.* **32**, 1460341 (2014)
- B. Tiss, M. Erouel, N. Bouguila, M. Kraini, K. Khirouni, J. Alloy. *Compd.* **771**, 60–66 (2019)
- N. Khatun, E. Rini, P. Shirage, P. Rajput, S. Jha, S. Sen, *Mater. Sci. Semicond. Process.* **50**, 7–13 (2016)
- A. Hafdallah, F. Yanineb, M. Aida, N. Attaf, In doped ZnO thin films. *J. Alloys Compd.* **509**, 7267–7270 (2011)
- K. Vanheusden, C.H. Seager, W.L. Warren, D.R. Tallant, J.A. Voigt, *Appl. Phys. Lett.* **68**, 403 (1996)
- A. Teke, U. Ozgur, S. Dogan, X. Gu, H. Morkoç, B. Nemeth, J. Mause, H.O. Everitt, *Phys. Rev. B* **70**, 195207 (2004)
- H. Kaftelen, K. Ocakoglu, R. Thomann, S. Tu, S. Weber, E. Erdem, *Phys. Rev. B* **86**(1), 014113 (2012)
- G. Jain, C. Rocks, P. Maguire, D. Mariotti, *Nanotechnology* **31**(21), 215707 (2020)
- M. Benamara, S.S. Teixeira, M.P.F. Graça, M.A. Valente, S.K. Jakka, H. Dahman, E. Dhahri, M. Debliquy, D. Lahem, *Appl. Phys. A* **127**(9), 1–15 (2021)
- C.G. Koops, *Phys. Rev.* **83**, 121–124 (1951)
- S. Lenaerts, J. Roggen, G. Maes, *Acta Part A* **51**, 883–894 (1995)
- N. Yamazoe, J. Fuchigami, M. Kishikawa, T. Seiyama, *Surf. Sci.* **86**, 335–344 (1979)
- X. Geng, J. You, C. Zhang, *J. Alloys Compd.* **687**, 286–293 (2016)
- A. Naldoni, M. Allieta, S. Santangelo, M. Marelli, F. Fabbri, S. Cappelli, C.L. Bianchi, R. Psaro, V. Dal Santo, *J. Am. Chem. Soc.* **134**, 7600–7603 (2012)
- B. Sarwana, B. Pare, A.D. Acharya, *Mater. Sci. Semicond. Process.* **25**, 89–97 (2014)
- X. Yang, H. Tao, W.R. Leow, J. Li, Y. Tan, Y. Zhang, T. Zhang, X. Chen, S. Gao, R. Cao, *J. Catal.* **373**, 116–125 (2019)
- Y. Qin, Z. Ye, *Sens. Actuators B Chem.* **222**, 499–507 (2016)
- S. Nadupalli, S. Repp, S. Weber, E. Erdem, *Nanoscale* **13**(20), 9160–9171 (2021)
- S. Repp, S. Weber, E. Erdem, *J. Phys. Chem. C* **120**(43), 25124–25130 (2016)
- C. Zhang, X. Geng, J. Lia, Y. Luoa, P. Lu, *Sens. Actuators B Chem.* **248**, 886–893 (2017)
- J.H. Jun, J. Yun, K. Cho, I.S. Hwang, J.H. Lee, S. Kim, *Sens. Actuators B Chem.* **140**, 412–417 (2009)
- C. Zhang, M. Debliquy, H. Liao, *Appl. Surf. Sci.* **256**, 5905–5910 (2010)
- S. Fan, A.K. Srivastava, V.P. Dravid, *Sens. Actuators B Chem.* **144**, 159–163 (2010)

57. R.K. Sonker, S.R. Sabhajeet, S. Singh, B.C. Yadav, *Mater. Lett.* **152**, 189–191 (2015)
58. L.S. Vlasenko, G.D. Watkins, *Phys. Rev. B* **71**, 125210 (2005)
59. L. Yu, F. Guo, S. Liu, B. Yang, Y. Jiang, L. Qi, X. Fan, *J. Alloys Compd.* **682**, 352–356 (2016)
60. R.R. Kumar, T. Murugesan, T.W. Chang, H.N. Lin, *Mater. Lett.* **287**, 129257 (2021)
61. Z. Liu, L. Yu, F. Guo, S. Liu, L. Qi, M. Shan, X. Fan, *Appl. Surf. Sci.* **423**, 721–727 (2017)
62. Y. Mun, S. Park, S. An, C. Lee, H.W. Kim, *Ceram. Int.* **39**(8), 8615–8622 (2013)
63. J. Wang, Y. Shen, X. Li, Y. Xia, C. Yang, *Sens. Actuators B Chem.* **298**, 126858 (2019)

Publisher's Note Springer Nature remains neutral with regard to jurisdictional claims in published maps and institutional affiliations.